ACS NANO

www.acsnano.org

ARTICLE

Ultraporous, Ultrasmall $MgMn_2O_4$ Spinel Cathode for a Room-Temperature Magnesium Rechargeable Battery

Hiroaki Kobayashi,* Yu Fukumi, Hiroto Watanabe, Reona Iimura, Naomi Nishimura, Toshihiko Mandai, Yoichi Tominaga, Masanobu Nakayama, Tetsu Ichitsubo, Itaru Honma, and Hiroaki Imai*

Cite This: *ACS Nano* 2023, 17, 3135–3142

Read Online

ACCESS | Metrics & More | Article Recommendations | Supporting Information

ABSTRACT: Magnesium rechargeable batteries (MRBs) promise to be the next post lithium-ion batteries that can help meet the increasing demand for high-energy, cost-effective, high-safety energy storage devices. Early prototype MRBs that use molybdenum-sulfide cathodes have low terminal voltages, requiring the development of oxide-based cathodes capable of overcoming the sulfide's low Mg^{2+} conductivity. Here, we fabricate an ultraporous (>500 m^2 g^{-1}) and ultrasmall (<2.5 nm) cubic spinel $MgMn_2O_4$ (MMO) by a freeze-dry assisted room-temperature alcohol reduction process. While the as-fabricated MMO exhibits a discharge capacity of 160 mAh g^{-1}, the removal of its surface hydroxy groups by heat-treatment activates it without structural change, improving its discharge capacity to 270 mAh g^{-1}—the theoretical capacity at room temperature. These results are made possible by the ultraporous, ultrasmall particles that stabilize the metastable cubic spinel phase, promoting both the Mg^{2+} insertion/deintercalation in the MMO and the reversible transformation between the cubic spinel and cubic rock-salt phases.

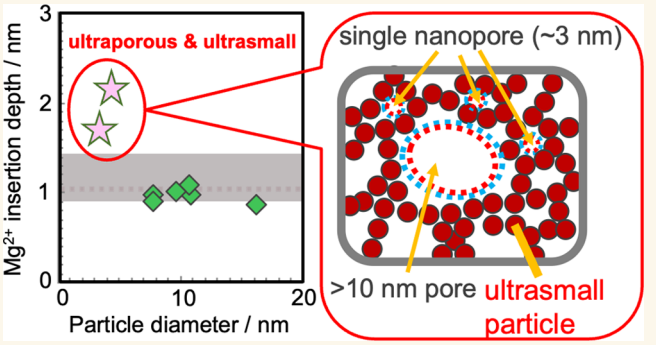

KEYWORDS: *magnesium battery, porous nanoparticles, cathode materials, cubic metastable spinel, freeze-drying*

With the growing number of portable electronics and electric vehicles, the demand for energy storage devices, such as lithium-ion batteries (LIBs), is ever-increasing.[1] To meet this demand for high-energy, cost-effective, and high-safety energy storage devices, new types of post-LIBs are always in development. To this end, magnesium rechargeable batteries (MRBs), have gained much attention: the abundant Mg metal undergoes safe anode reactions with a predicted volumetric capacity much higher than that of the expensive and reactive Li metal.[2−4]

Previously, a working MRB prototype that uses Mo_6S_8 Chevrel-type cathode, Mg metal anode, and Grignard-type electrolyte had been reported by Aurbach et al.[5] However, this prototype showed an operating voltage of ∼1.1 V, a low value attributed to the transition metal sulfide-type cathode materials. Because transition-metal-oxide materials, such as layered,[6] tunnel,[7] and spinel-type[8−10] oxides are predicted to have higher potentials than sulfides, these materials are the prime candidates for the next MRB cathode material.

Among the transition metal oxides, the spinel $MgMn_2O_4$ (MMO) has a suitably high theoretical energy density.[11,12] However, its conductivity is low due to the strong interactions between Mg^{2+} and O^{2-}.[13] Our previous density functional theory (DFT) studies has indicated that the Mg^{2+} diffusion coefficients at 298 K in the cubic MMO (6.4×10^{-15} cm^2 s^{-1})[14] to be 10^6 times lower than the Li^+ diffusion coefficient in the similar cubic spinel $LiMn_2O_4$ (4.7×10^{-9} cm^2 s^{-1}).[15] Very recently, an extended mixed conduction theory has indicated that the Mg^{2+} diffusion coefficient in $MgCr_2O_4$ is comparable to the Li^+ diffusion, but its conductivity is still estimated at low value.[16] A large polarization due to the low conductivity is expected to cause unwanted effects such as poor energy efficiency and oxidative electrolyte decomposition (>3.5 V vs Mg in glyme-based common electrolytes). Some reports suggest that the Mg insertion/deintercalation in MMO is accelerated by water addition into the electrolyte.[6,17] However,

Received: December 14, 2022
Accepted: January 18, 2023
Published: January 20, 2023

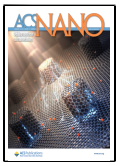

this approach is not applicable to MRBs due to Mg deposition/dissolution at the anode. Therefore, the successful replacement of magnesium sulfides by MMOs in MRBs depends on the use of electrolytes that is compatible with both the cathode and the anode.

Here, we demonstrate high-voltage MRB full cells; we fabricate highly porous nanosized oxides to reduce the Mg conduction path in the MMO cathode material, an approach that was previously attempted by many groups.[12] Recently, our group has developed porous MMO nanoparticles (~8 nm diameter) with a specific surface area (SSA) of ~250 $m^2\ g^{-1}$ by a sol–gel process,[18] and ultrasmall MMO nanoparticles (<5 nm) with a SSA of ~150 $m^2\ g^{-1}$ by alcohol reduction process,[19] which all showed a first discharge capacity of 230 mAh g^{-1} at room temperature. This discharge value, while high among MMO cathodes, was still 85% of the theoretical capacity (270 mAh g^{-1}). To enhance the cathode performance and achieve the theoretical capacity, the addition of porosity to the ultrasmall MMO nanoparticles is a possible strategy. In this work, we enhance the cathode performance by increasing the porosity of the MMO. We fabricate ultraporous, ultrasmall MMO cathode nanoparticles and demonstrate a first discharge capacity of 270 mAh g^{-1}, i.e., the theoretical capacity at room temperature.

RESULTS AND DISCUSSION

Phase Stability and Migration Energy of Mg Hopping between the Spinel and Rock-Salt Phases. First, we investigate the theoretical effects of the Mg^{2+} insertion reaction on the MMO cathode. Figure 1a shows the DFT-calculated formation energies for $Mg_xMn_2O_4$ ($1 \le x \le 2$) with varying Mg/vacancy configurations, where the total energies of both extremes of the compositional range ($x = 1$ and 2) are set to 0. The lowest energy configurations for $MgMn_2O_4$ and $Mg_2Mn_2O_4$ ($x = 1$ and 2) are confirmed to be the spinel and the rock-salt structures, respectively, where all Mg ions occupy the tetrahedral and the octahedral sites. All the formation energies for $Mg_xMn_2O_4$ ($1 \le x \le 2$) cells are positive, indicating a two-phase transformation reaction between the spinel $MgMn_2O_4$ ($x = 1$) and the rock-salt $Mg_2Mn_2O_4$ ($x = 2$). The calculated reaction potential for the two-phase transformation is 1.68 V (vs Mg^{2+}/Mg).

The kinetics of two-phase transformation reactions are often slow, since these reactions involve both nucleation and growth processes that accompany phase-boundary motions. However, Malik et al. have suggested previously[20] that the kinetically feasible single-phase transformation pass (i.e., solid solution reaction) for the olivine-type $LiFePO_4$–$FePO_4$ system shows ultrafast reaction kinetics[21] despite the two-phase coexistence reaction system. The availability of the single-phase transformation pass is attributed to small formation energies for the intermediate compositions, corresponding to very small overpotential. Note that both $MgMn_2O_4$ and $Mg_2Mn_2O_4$ structures consist of the same structure flamework of Mn_2O_4, where oxide ions form cubic closed packing structure and Mn ions located at the octahedral sites. Mg ions occupy tetrahedral sites or octahedral sites in $MgMn_2O_4$ or $Mg_2Mn_2O_4$ structures, and both Mg sites are on the 3-dimensional diffusion path. Hence, a single-phase transformation pass is also available for the $MgMn_2O_4$–$Mg_2Mn_2O_4$ two phase coexistence system. However, the formation energy profile in Figure 1a, relatively large overpotential (>1 V) at the onset of discharge reaction (at the compositional range, $1 \le x \le 1.25$, in $Mg_xMn_2O_4$) is

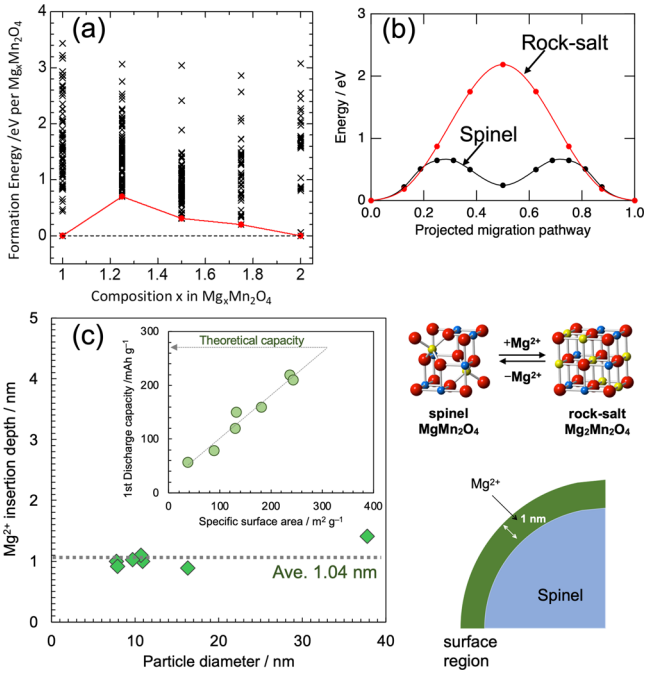

Figure 1. (a) DFT-calculated formation energies as a function of composition x in $Mg_xMn_2O_4$ ($1 \le x \le 2$) with varying Mg/vacancy arrangement. The hatched line corresponds to the convex hull. (b) Energy profile during Mg^{2+} ion migration in rock-salt $Mg_2Mn_2O_4$ (red curve) and spinel $MgMn_2O_4$ (black curve).[14] (c) Correlation between the particle diameter of the nanostructured MMO and the Mg insertion depth published in our previous work.[18] The inset shows the correlation between the SSA and the first discharge capacity.

required to realize single-phase transformation reaction. Accordingly, the reaction should proceed via the two-phase transformation pass between the spinel $MgMn_2O_4$ and the rock-salt $Mg_2Mn_2O_4$.

Previously, we reported that the Mg migration energy for the cubic MMO is 0.67 eV, indicating that Mg^{2+} diffusion is kinetically possible at a 1C-rate, even at 25 °C, via nanoscale particle synthesis.[14] The estimated migration energy agree well with muon spin relaxation (μSR) studies (~0.7 eV), and powder diffraction and solid-state NMR studies (~0.69 eV).[22] In addition, former DFT-NEB studies for $MgMn_2O_4$ and relatives shows the comparable migration energies ranging from 0.49 eV to ~0.78 eV).[22−26] However, the Mg migration energy for the reduced phase, i.e. rock-salt $Mg_2Mn_2O_4$ is expected to be much larger. Figure 1b compares the DFT-NEB derived energy profiles of Mg migrations in rock-salt $Mg_2Mn_2O_4$ and spinel $MgMn_2O_4$. In rock-salt, the straight pass shows the lowest migration energy compared with the bending passes via both tetrahedral vacancy sites (Figure S1). The migration energy in rock-salt is 2.2 eV, which is about three times larger than that in spinel.[14] This route is different from the spinel $MgMn_2O_4$; the energy maximum is at the middle of the migration pass, adjacent to two oxide ions. Hence, the repulsive interactions from the overlap of electron clouds between the hopping Mg and the neighboring oxide ions may be the primary reason for the large migration energy.

According to the migration energies, the diffusion coefficients of Mg at 298 K for rock-salt $Mg_2Mn_2O_4$ are approximately 10^{-40} $cm^2\ s^{-1}$. In other words, the diffusion distance at 298 K for rock-salt $Mg_2Mn_2O_4$ corresponds to

https://doi.org/10.1021/acsnano.2c12392
ACS Nano 2023, 17, 3135−3142

approximately 10^{-11} nm per hour as dictated by random walk theory. Because the discharge reaction of MMO is determined to be a two-phase transformation reaction, the partial Mg insertion into the MMO surface at the initial discharge step is expected to form the $MgMn_2O_4$-core/$Mg_2Mn_2O_4$-shell structure, preventing further Mg uptake due to the slow Mg diffusion in the rock-salt $Mg_2Mn_2O_4$-shell phase. This scenario had been observed in systems such as the $MgCo_2O_4$ electrode materials.[10,27]

However, our previously developed porous MMO nanoparticles[18] have a Mg insertion depth of ∼1 nm at room-temperature (Figure 1c). This suggests that at the near surface regions (∼1 nm), Mg insertion can proceed faster than theoretically predicted due to the instabilities at these regions. In other words, ultrasmall MMO nanoparticles with ∼2 nm diameter should exhibit the full transformation to rock-salt $Mg_2Mn_2O_4$ at discharge. Further, our previous study shows that nanosized spinel $LiMn_2O_4$ undergo fast Li insertion without formation of the core−shell structure.[28] To enable the Mg insertion into the bulk spinel $MgMn_2O_4$, downsizing the active materials to the ultrasmall-scale to prevent the core−shell structure formation is essential. In addition, the discharge capacity of MMO strongly depends on the SSA (inset of Figure 1c). The complete discharge is also achievable using ultraporous MMO with SSA of ∼300 m^2 g^{-1}. Since the aggregates should inhibit the Mg insertion into cores, epoch-making synthesis of ultraporous and ultrasmall MMO nanoparticles is required.

Suppressing Aggregation to Enhance the Specific Surface Area of Ultrasmall Nanoparticles. First, we study the particle size of the primary nanoparticle structure by synthesizing the MMO nanoparticles following our procedure.[19] The transmission electron microscopy (TEM) image of the resulting product in Figure 2a shows MMO particles as dark spots with an average size of 2.1 nm dispersed throughout the image. Using the MMO density of 4.67 g cm^{-3} from the X-ray diffraction (XRD) Rietveld analysis (Figure S2), we estimate the SSA to be 610 m^2 g^{-1}, a large value among oxides in general.

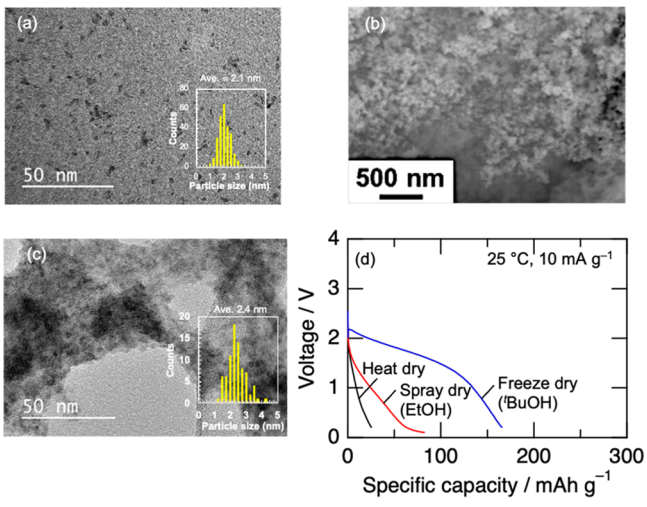

Figure 2. (a) TEM image of MMO particles obtained from the diluted condition. (b) SEM and (c) TEM images of the freeze-dried MMO particles from the ᵗBuOH dispersion. (d) Discharge curves of MMO cathodes prepared using the three different drying processes.

Entry 1 in Table 1 indicates that the Brunauer−Emmett−Teller (BET) SSA of our MMO previously prepared in ref 19

Table 1. BET SSA of MMOs Prepared Using Different Drying and Dispersion Processes

Entry	Drying process	Dispersion	Specific surface area (m^2 g^{-1})
1[a]	Heat-drying		151[19]
2	Heat-drying		308
3	Freeze-drying	Water	293
4	Freeze-drying	Cyclohexane	73
5	Freeze-drying	ᵗBuOH	506
6	Spray-drying	Water	114
7	Spray-drying	EtOH	155

[a]Without addition of glyme.

was only 151 m^2 g^{-1}, due to aggregation of the unstable ultrasmall particles during the drying process. In this work, we suppress this aggregation by changing both the reaction solvent and the drying process. As we have stated previously,[19,29] the MMO formation reaction is water-sensitive; water contamination should form a less-reactive Mg^{2+} aqua complex, producing either the todorokite-type Mg-OMS-1, or Mn_3O_4. Glyme is a well-known electrolyte that interacts with metal cations to form stable cation-glyme complex. Mixing glyme into the solution can effectively suppress the formation of Mg^{2+} aqua complex, obtaining MMO. In addition, the glyme mixing to the solution is also effective to increase the SSA of spinels, probably due to surface stabilizing effect to prevent an aggregation of the particles. This has been demonstrated by Nakai et al., who succeeded in increasing the SSA of Co−Mn spinel from 338 to 425 m^2 g^{-1} by only changing the reaction solvent—adding glyme to the alcohol solution.[30,31] In the present work, the SSA of the MMO prepared using the glyme-alcohol mixture (Entry 2 in Table 1) has been practically doubled without any change in XRD patterns (Figure S3).

Next, we study the control of the secondary porous particle structure. As the first and second steps in the Figure S4 scheme illustrate, the MMO suspension is intentionally aggregated and precipitated by adding a small amount of water as a flocculant. At this stage, the particles are weakly aggregated via the intermediate of water. The third and fourth steps in the Figure S4 scheme involve the strong aggregation by drying. Here, we compare several drying techniques to control the strong aggregation. We applied the freeze-drying process that is commonly used to produce ceramics with complex pore structure with several dispersion liquids.[32] As Table 1 indicates, while the freeze-dried MMO from the water dispersion (Entry 3) show almost similar SSA from the heat-drying method (Entry 2), the freeze-dried MMO from the cyclohexane dispersion (Entry 4) considerably decreased SSA (73 m^2 g^{-1}). In contrast, the freeze-dried MMO from the *tert*-butyl alcohol (ᵗBuOH) dispersion (Entry 5) exhibits the greatest improvement with a SSA of 506 m^2 g^{-1}. The result in Entry 4 is likely caused by an accelerated nanoparticle aggregation by dispersion of the hydrophilic MMO into the hydrophobic cyclohexane.

We investigate the hierarchical structures obtained using the Entry 5 method. The scanning electron microscopy (SEM) image in Figure 2b shows the resulting porous networks that is composed of secondary structures of tens of nanometer in average size. Further, the TEM image in Figure 2c shows that the secondary particles are the results of aggregated primary

https://doi.org/10.1021/acsnano.2c12392
ACS Nano 2023, 17, 3135−3142

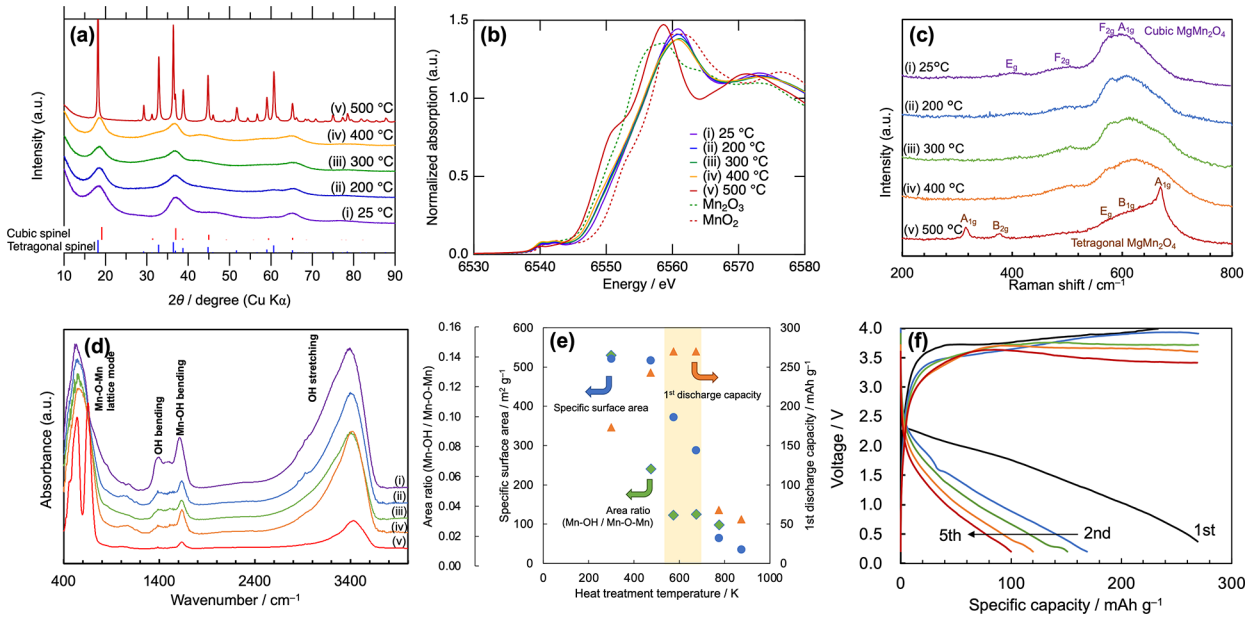

Figure 3. Heat-treatment of the freeze-dried MMO particles from ^{t}BuOH dispersion. (a) XRD, (b) Mn K-edge XANES, (c) Raman, and (d) FT-IR spectra showing the effects of the heat treatment on MMO. (e) Summary of the FT-IR peak-area ratios (Mn−OH/Mn−O−Mn), SSA, and first discharge capacity. (f) Voltage curves of the MMO after heat treatment at 300 °C.

particles with an average size of 2.4 nm. According to the pore-size distribution analyzed by using Barrette-Joynere-Halenda (BJH) method (Figure S5), the hierarchical structure has nanopores of around 4 nm, and macropores. This bimodal porous network—with nano- and micropores—is formed by the weak aggregation of primary and secondary particles, respectively, keeping the interparticle voids. The strong interactions between MMO particles via water are reduced by substitution with ^{t}BuOH, resulting in the ultraporous structure.

We also applied the spray-drying process, which is often used to granulate nanoparticles of ceramics.[33] The spray-dried MMO powders show spherical morphology (Figure S6), which is different from the freeze-dried MMO powders. The secondary particle size is dependent on dispersants; 5−20 μm in water and 2−5 μm in ethanol (EtOH). The SSA of the structures obtained by the spray-drying process significantly decreased to 100−150 $m^2\ g^{-1}$ (Entries 6 and 7 in Table 1).

After fine-tuning the MMO using the above methods, we test the overall MRB performances of the MMO cathodes using the coin-type full cells, composed of Mg anode and $Mg[B(HFIP)_4]_2$/triglyme (HFIP: hexafluoroisopropyl) electrolyte. Figure 2d shows the first discharge curves comparing the MMO obtained from different drying methods. As the black and red curves in Figure 2d indicate, the heat- and spray-dried MMO exhibit no discharge plateau, with the discharge capacities of only 20 and 60 mAh g^{-1}, respectively, probably due to the strong aggregation of MMO particles. The blue curve in Figure 2d indicates that the freeze-dried MMO exhibits a 2 V-discharge plateau, suggesting that Mn reduction has occurred. The discharge capacity, however, is 160 mAh g^{-1}, which is much lower than the theoretical capacity of MMO (270 mAh g^{-1}) predicted from the large SSA (inset in Figure 1c). Since there is no calcination step in the MMO preparation, the hydroxy groups on the ultraporous particles surface should be present. These hydroxy groups may inhibit the discharge reaction.

Surface Functionalization of MMO by Heat Treatments. To remove the surface hydroxy groups, we apply heat treatment to the ^{t}BuOH-freeze-dried MMO. The thermogravimetry (TG) curve of MMO in Figure S7 shows a gradual weight decrease as the temperature is ramped up to 300 °C, followed by a sudden weight loss at 500 °C. According to the XRD in Figure 3a, while no major structural change is observed during the gradual weight decrease, the MMO undergoes drastic structural change after the sudden weight loss. Because the alcohol reduction process is a room-temperature synthesis, the resulting MMO is a room-temperature metastable phase; XRD Rietveld fitting (Figure S2) and inductively coupled plasma atomic emission spectroscopy (ICP-AES) analyses indicate that the obtained MMO is a Mg-site defect nonstoichiometric cubic spinel $Mg_{0.72}Mn_2O_4$. The Rietveld analysis also shows the MMO treated at 400 °C retains its cubic spinel structure (Figure S8a). After the heat treatment at 500 °C, the cubic spinel transform to tetragonal spinel $(Mg_{0.8}Mn_{0.2})Mn_2O_4$ by releasing O_2 (Figure S8b).

Figure 3b shows Mn *K*-edge X-ray absorption near edge structure (XANES) spectra acquired on MMO throughout the heat treatment. The edge energy of MMO before heat treatment was between Mn_2O_3 and MnO_2, indicating the mixed valence state of Mn^{3+} and Mn^{4+}. The existence of Mn^{4+} supports the estimated nonstoichiometric formula. After heat treatment, the edge energy shifted to lower energy; reduction of Mn^{4+} proceeds by the heat treatment. The trend in the energy shift is also observed in Mn 2p X-ray photoelectron spectra (XPS) (Figure S9).

Figure 3c shows the Raman spectra acquired on MMO throughout the heat treatment. Spectrum i (before heat-treatment) shows a broad peak with a shoulder and two weak peaks. Comparing this spectrum to that of the cubic $LiMn_2O_4$[34] and other tetragonal Mn spinels,[35] we assign these signals to the cubic spinel phase. We attribute the broad signal around 615 cm^{-1} to the symmetric stretching Mn−O vibration of MnO_6 octahedra with A_{1g} symmetry mode; the

https://doi.org/10.1021/acsnano.2c12392
ACS Nano 2023, 17, 3135−3142

shoulder at 580 cm^{-1} to the stretching of symmetry mode F_{2g}; and the weak signals to the F_{2g} and E_g mode. Spectrum iv in Figure 3c shows that after heating at 400 °C, while the F_{2g} signal has decreased in intensity, the A_{1g} signal has increased in intensity. This result suggests the reduction of Mn^{4+} by heat treatment. Spectrum v in Figure 3c shows that after heating at 500 °C, all Raman signals from the cubic spinel phase are no longer observable, replaced by a set of signals located at 666, 375, and 313 cm^{-1}; we assign these signals to the tetragonal MMO spinel phase[35] and attribute them to the vibrations of A_{1g}, B_{2g}, and A_{1g} symmetry mode, respectively. The combined results from the Raman measurements indicate that the thermal phase transition from the cubic to the tetragonal MMO takes place above 500 °C.

Figure 3d shows the Fourier-transform infrared (FT-IR) spectra acquired on MMO throughout the heat treatment. We attribute the signal at 600 cm^{-1} to the Mn−O−Mn lattice vibration and the signal at 3200 cm^{-1} to the OH stretching mode both of the surface Mn−OH groups and of adsorbed water. We attribute the signals at 1600 and 1400 cm^{-1} to the OH bending modes both of the surface Mn−OH groups and of adsorbed H_2O. Spectra ii−v in Figure 3d show that after the heating at 200 °C, the signals related to −OH vibrations are significantly decreased.

Figure 3e summarizes the correlation between the heat treatment temperatures and the integrated Mn−OH:Mn−O−Mn peak area ratio: the ratio decreases with increasing temperature. This result indicates that the heat treatment above 300 °C removes the surface Mn−OH groups. Figure 3e also summarizes the correlations between the heat treatment temperatures and both the SSAs (isotherms were plotted in Figure S10). and the first discharge capacities of the MMO (voltage curves were plotted in Figure S11). Up to 400 °C, while the SSA decreases gradually from 506 to 300 $m^2\ g^{-1}$, indicating the presence of both nanopores and macropores (Figure S12a), the discharge capacity greatly increases to reach the theoretical capacity of 270 mAh g^{-1} at 300−400 °C, where the surface Mn−OH groups are effectively removed. Electrochemical impedance spectroscopy (EIS) confirmed the decrease in charge transfer resistance by eliminating surface hydroxy groups (Figure S13). Figure 3e also shows that after the heat treatment at 500 °C, the SSA is drastically reduced to below 100 $m^2\ g^{-1}$, indicating the complete disappearance of nanopores (Figure S12b). Similarly, the discharge capacities are also reduced to 56 mAh g^{-1}, due to the major structural changes and low SSA.

Figure 3f shows the discharge/charge cycles of the MMO treated at 300 °C. We previously confirmed the electrolyte decomposition at the same cell test condition by XPS analysis.[36] Although the decomposition of electrolyte occurred competitively during overcharge, but we performed the cell test with the voltage range of 0.1−4.0 V to proceed the oxidation reaction. The discharge capacity gradually decreases due to the side reaction of electrolyte decomposition at the charge step; the cathode can be well cycled using the high-voltage stable electrolyte.

Figure 4a shows the calculated Mg^{2+} insertion depths of the ultraporous and ultrasmall MMO treated at 300 and 400 °C. The particle diameters were calculated using the SSA. The calculated insertion depths are longer than that of the previously reported porous tetragonal MMO nanoparticles.[18] We attribute this improvement to the specific crystal phase: the ultrasmall MMO is a metastable cubic spinel phase. According to previous literature, this phase can be obtained in the ultrasmall (<7 nm) particle range.[14,19] The Mg^{2+} insertion into MMO results in a formation of the cubic rock-salt $Mg_2Mn_2O_4$ during the discharge process. Though the Mg^{2+} migration energy is almost same between the cubic and the tetragonal MMOs, the phase transition from the cubic (spinel) to the cubic (rock-salt) is much faster than that from tetragonal (spinel) to cubic (rock-salt) because of the absence of the lattice distortion change during the Mg insertion. This is the key point that explains the higher performances of the cubic spinel MMOs compared to the tetragonal MMOs.

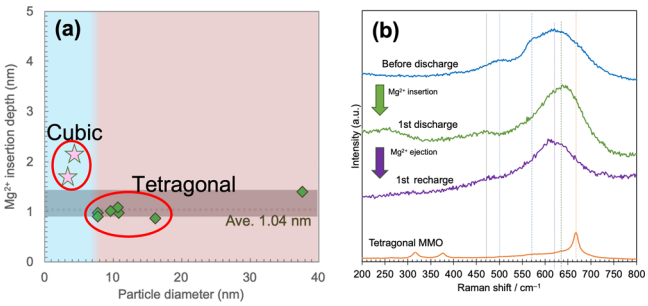

Figure 4. (a) Estimated Mg insertion depth of the MMO. (b) Raman spectra of the MMO during discharge−charge.

Figure 4b shows the Raman spectra acquired on the MMO electrode during first cycle. After the first discharge, the strong broad peak at 580 cm^{-1} that indicates the high Mn^{4+} contents has decreased, suggesting Mn reduction. Further, the peak position of the A_{1g} mode has shifted to a higher frequency due to the Mg insertion. After charging, the peak position of the A_{1g} mode has shifted back to the original position of the sample before discharge. After the first discharge/charge, the intensity of the MMO F_{2g} mode has decreased compared to the original sample before discharge. This is because the voltage applied in the present system can only induce the electrochemical oxidation from Mn^{2+} to Mn^{3+}. Notably, the tetragonal spinel phase is not observed through the discharge/charge processes, suggesting that reversible transition between the cubic spinel and the cubic rock-salt has occurred; in the ultrasmall region, the cubic MMO phase is rather stable than tetragonal MMO phase. This observation should play an important role in the smooth insertion/ejection of Mg^{2+} ions, resulting in a longer Mg^{2+} insertion depth.

CONCLUSIONS

We have fabricated a ultraporous (>500 $m^2\ g^{-1}$), ultrasmall (<2.5 nm) cubic spinel $MnMn_2O_4$ (MMO) by freeze-dry assisted room-temperature alcohol reduction process. We have determined that the resulting MMO nanoparticles have hydroxy groups at surfaces, which can be removed by a subsequent heat-treatment at 300−400 °C without structural change. We have tested the hydroxy-free MMO cathode and found a high discharge capacity of 270 mAh g^{-1}, corresponding to its theoretical capacity. The ultrasmall particles stabilize the metastable cubic spinel phase, enabling both the Mg^{2+} insertion into the MMO core and the reversible transformation between cubic spinel and cubic rock-salt MMO phases.

METHODS

Computational Method. First-principles DFT calculations were used to investigate both the phase stabilities between the spinel $MgMn_2O_4$ and the rock-salt $Mg_2Mn_2O_4$ structures, and the ion-

https://doi.org/10.1021/acsnano.2c12392
ACS Nano 2023, 17, 3135−3142

migration property of Mg ions in $Mg_2Mn_2O_4$. For the crystal structure input of the spinel $MgMn_2O_4$, the $I4_1/amd$ space group suggested by both refs.[14] and,[37] where all the Mg and Mn ions are located at tetrahedral and octahedral sites, was used. To evaluate the total energies for compounds after the topochemical Mg insertions (i.e., $Mg_xMn_2O_4$ ($1 < x \leq 2$)), the ATAT software package[38] was used to produce a total of 513 symmetrically distinct Mg/vacancy arrangements. The DFT calculations for the total energies, formation energies and voltages were performed according to previous reports.[9,39] A combination of the projector augmented-wave (PAW) method,[40] plane-wave basis set, and a generalized gradient approximation (GGA)-type exchange-correlation functional developed by Perdew, Burke, and Ernzernhof modified for solid materials (PBEsol)[41,42] was used as implemented in the Vienna Ab Initio Simulation Package (VASP).[43,44] The on-site Coulomb correction (GGA+U) was used to describe the localized electronic states in the Mn 3d orbital ($U_{Mn,d}$ = 3.9 eV[45]). The nudged elastic band (NEB) method[46] was applied to evaluate the minimum energy pathways of the Mg jump in the rock-salt $Mg_2Mn_2O_4$. In detail, the model cell consisted of the superstructure of the $2 \times 2 \times 2$ conventional rock-salt structure with a single Mg vacancy as migration species (i.e., $Mg_{15}Mn_{16}O_{32}$). Unless mentioned otherwise, we refer to the Mg vacancy-containing superstructure as $Mg_2Mn_2O_4$.

Sample Preparation. $MgMn_2O_4$ (MMO) was prepared using the modified alcohol reduction process.[19,36] $(n\text{-Bu})_4NMnO_4$ was prepared according to a previous report.[47] 2 mmol of $(n\text{-Bu})_4NMnO_4$ powder was first slowly added to a 2 mmol $MgCl_2$ solution made in a 25 mL ethanol and 25 mL diglyme mixture under vigorous stirring for 1 h. Ten milliliters of water was then injected to the brown colloidal solution, precipitating the MMO. The precipitate was filtered or centrifuged, followed by washing with ethanol several times to obtain the MMO wet cake, which was then dried using three different techniques: (i) heat-dried at 120 °C in air overnight; (ii) dispersed into solvents (water, cyclohexane, or *tert*-butyl alcohol) followed by freeze-drying using DC401 (Yamato Scientific Co., Ltd.); and (iii) dispersed into solvents (water or ethanol), followed by spray-drying under N_2 atmosphere using ADL311S-A (Yamato Scientific Co., Ltd.) connected with solvent recovery unit (GAS 410, Yamato Scientific Co., Ltd.).

Materials Characterization. The scanning electron microscopy (SEM) images were obtained using JSM-7100F or JSM-7800F. The transmission electron microscopy (TEM) images were obtained using FEI Tecnai G2. The X-ray diffraction (XRD) patterns were obtained using a Bruker D2 PHASER XE-T Edition. The Rietveld refinement was performed using the RIETAN-FP program.[48] The Brunauer–Emmett–Teller (BET) specific surface areas were measured by N_2 adsorption at 77 K using a BELSORP MAX G (MicrotracBEL) or 3Flex-3MP (Micromeritics). Samples were degassed at 100 °C for 12 h under vacuum. Elemental analysis was performed using inductively coupled plasma atomic emission spectroscopy (ICP-AES, Shimadzu ICPE- 9000). Thermogravimetric analysis (TG) was performed using TG-DTA2000S (Netzsch). Raman and Fourier Transform Infrared (FT-IR) spectra were obtained using InVia Raman Microscope (Renishaw) and FT/IR-4200typeA (JASCO), respectively. X-ray absorption spectroscopy (XAS) in the transmission method was performed at the AichiSR. Spectra were analyzed using Athena.[49] X-ray photoelectron spectroscopy (XPS) was conducted using a PHI 5000 VersaProbe II.

Electrochemical Tests. The samples were mixed with acetylene black (AB; Denka Black, FX-35, Denka Co., Ltd.) and polytetrafluoroethylene (PTFE; Teflon, 6-J, DuPont-Mitsui Fluorochemicals Co., Ltd.) at a respective weight ratio of 60:30:10. These mixtures were cut into 8 mm diameter disks of typically 2.5 mg and pressed onto an Al mesh current collector to serve as cathodes. The electrodes were dried at 160 °C under vacuum and introduced into an Ar-filled glovebox. The cathode and the Mg–Al–Zn alloy (AZ-31, Nippon Kinzoku Co., Ltd.) anode, and 0.3 M $Mg[B(HFIP)_4]_2$/triglyme (HFIP: hexafluoroisopropyl) electrolyte[50] were assembled in a 2032 coin-type cell (Hohsen Corp.) with a glass-fiber separator (GA-100, Toyo Roshi Kaisha, Ltd.). The charge/discharge tests were performed at 25 °C in the constant-current (CC) mode using either a multichannel potentiostat system (VMP3, Bio-Logic Science Instruments), or a battery test system (HJ-1001SD8, Hokuto Denko Corp.). Electrochemical impedance spectroscopy (EIS) was performed using an activated carbon counter electrode instead of the Mg anode.

ASSOCIATED CONTENT

Supporting Information

The Supporting Information is available free of charge at https://pubs.acs.org/doi/10.1021/acsnano.2c12392.

Results of the theoretical calculations, XRD Rietveld refinements, pore distributions, XPS, SEM analysis, electrochemical tests (PDF)

AUTHOR INFORMATION

Corresponding Authors

Hiroaki Kobayashi – *Institute of Multidisciplinary Research for Advanced Materials, Tohoku University, Sendai, Miyagi 980-8577, Japan*; orcid.org/0000-0001-6705-9515; Email: h.kobayashi@tohoku.ac.jp

Hiroaki Imai – *Department of Applied Chemistry, Faculty of Science and Technology, Keio University, Yokohama, Kanagawa 223-8522, Japan*; orcid.org/0000-0001-6332-9514; Email: hiroaki@applc.keio.ac.jp

Authors

Yu Fukumi – *Department of Applied Chemistry, Faculty of Science and Technology, Keio University, Yokohama, Kanagawa 223-8522, Japan*

Hiroto Watanabe – *Department of Applied Chemistry, Faculty of Science and Technology, Keio University, Yokohama, Kanagawa 223-8522, Japan*

Reona Iimura – *Institute of Multidisciplinary Research for Advanced Materials, Tohoku University, Sendai, Miyagi 980-8577, Japan*

Naomi Nishimura – *Graduate School of Bio-Applications and Systems Engineering, Tokyo University of Agriculture and Technology, Koganei, Tokyo 184-8588, Japan*

Toshihiko Mandai – *Center for Green Research on Energy and Environmental Materials, National Institute for Materials Science (NIMS), Tsukuba, Ibaraki 305-0044, Japan*; orcid.org/0000-0002-2403-7794

Yoichi Tominaga – *Graduate School of Bio-Applications and Systems Engineering, Tokyo University of Agriculture and Technology, Koganei, Tokyo 184-8588, Japan*; orcid.org/0000-0001-5098-8537

Masanobu Nakayama – *Department of Advanced Ceramics, Nagoya Institute of Technology, Nagoya, Aichi 466-8555, Japan*; orcid.org/0000-0002-5113-053X

Tetsu Ichitsubo – *Institute for Materials Research, Tohoku University, Sendai, Miyagi 980-8577, Japan*

Itaru Honma – *Institute of Multidisciplinary Research for Advanced Materials, Tohoku University, Sendai, Miyagi 980-8577, Japan*

Complete contact information is available at: https://pubs.acs.org/10.1021/acsnano.2c12392

Author Contributions

H.K.: Conceptualization in ultrasmall particle application, writing manuscript -draft, project administration. Y.F.: Investigation in ultraporous particles fabrication and battery tests. H.W.: Analyses in Raman and FT-IR spectroscopies, writing manuscript -draft. R.I.: Validation in ultrasmall and

https://doi.org/10.1021/acsnano.2c12392
ACS Nano 2023, 17, 3135–3142

ultraporous particles fabrication and battery tests. N.N.: Investigation in spray drying. T.M.: Electrolyte supply. Y.T.: Methodology in spray drying. M.N.: Theoretical calculation. T.I.: Methodology in theoretical model. I.H.: Supervision. H.I.: Conceptualization in ultraporous particle application, supervision, project administration. All coauthors contributed to writing manuscript - review and editing.

Notes

The authors declare no competing financial interest.

ACKNOWLEDGMENTS

This work was supported by JST ALCA-SPRING (JPMJAL1301). This work was partially supported by JSPS KAKENHI (JP20H02436). We also thank Patrick Han for English editing.

REFERENCES

(1) Tarascon, J. M.; Armand, M. Issues and Challenges Facing Rechargeable Lithium Batteries. *Nature* **2001**, *414*, 359−367.
(2) Muldoon, J.; Bucur, C. B.; Gregory, T. Fervent Hype behind Magnesium Batteries: An Open Call to Synthetic Chemists—Electrolytes and Cathodes Needed. *Angew. Chem., Int. Ed.* **2017**, *56*, 12064−12084.
(3) Bucur, C. B.; Gregory, T.; Oliver, A. G.; Muldoon, J. Confession of a Magnesium Battery. *J. Phys. Chem. Lett.* **2015**, *6*, 3578−3591.
(4) Yoo, H. D.; Shterenberg, I.; Gofer, Y.; Gershinsky, G.; Pour, N.; Aurbach, D. Mg Rechargeable Batteries: An On-Going Challenge. *Energy Env. Sci.* **2013**, *6*, 2265−2279.
(5) Aurbach, D.; Lu, Z.; Schechter, A.; Gofer, Y.; Gizbar, H.; Turgeman, R.; Cohen, Y.; Moshkovich, M.; Levi, E. Prototype Systems for Rechargeable Magnesium Batteries. *Nature* **2000**, *407*, 724−727.
(6) Sun, X.; Duffort, V.; Mehdi, B. L.; Browning, N. D.; Nazar, L. F. Investigation of the Mechanism of Mg Insertion in Birnessite in Nonaqueous and Aqueous Rechargeable Mg-Ion Batteries. *Chem. Mater.* **2016**, *28*, 534−542.
(7) Hatakeyama, T.; Li, H.; Okamoto, N. L.; Shimokawa, K.; Kawaguchi, T.; Tanimura, H.; Imashuku, S.; Fichtner, M.; Ichitsubo, T. Accelerated Kinetics Revealing Metastable Pathways of Magnesiation-Induced Transformations in MnO_2 Polymorphs. *Chem. Mater.* **2021**, *33*, 6983−6996.
(8) Okamoto, S.; Ichitsubo, T.; Kawaguchi, T.; Kumagai, Y.; Oba, F.; Yagi, S.; Shimokawa, K.; Goto, N.; Doi, T.; Matsubara, E. Intercalation and Push-Out Process with Spinel-to-Rocksalt Transition on Mg Insertion into Spinel Oxides in Magnesium Batteries. *Adv. Sci.* **2015**, *2*, 1500072.
(9) Shimokawa, K.; Atsumi, T.; Okamoto, N. L.; Kawaguchi, T.; Imashuku, S.; Wagatsuma, K.; Nakayama, M.; Kanamura, K.; Ichitsubo, T. Structure Design of Long-Life Spinel-Oxide Cathode Materials for Magnesium Rechargeable Batteries. *Adv. Mater.* **2021**, *33*, 2007539.
(10) Shimokawa, K.; Atsumi, T.; Harada, M.; Ward, R. E.; Nakayama, M.; Kumagai, Y.; Oba, F.; Okamoto, N. L.; Kanamura, K.; Ichitsubo, T. Zinc-Based Spinel Cathode Materials for Magnesium Rechargeable Batteries: Toward the Reversible Spinel−Rocksalt Transition. *J. Mater. Chem. A* **2019**, *7*, 12225−12235.
(11) Mao, M.; Gao, T.; Hou, S.; Wang, C. A Critical Review of Cathodes for Rechargeable Mg Batteries. *Chem. Soc. Rev.* **2018**, *47*, 8804−8841.
(12) Michail, A.; Silván, B.; Tapia-Ruiz, N. Progress in High-Voltage $MgMn_2O_4$ Oxyspinel Cathode Materials for Mg Batteries. *Curr. Opin. Electrochem.* **2022**, *31*, 100817.
(13) Huie, M. M.; Bock, D. C.; Takeuchi, E. S.; Marschilok, A. C.; Takeuchi, K. J. Cathode Materials for Magnesium and Magnesium-Ion Based Batteries. *Coord. Chem. Rev.* **2015**, *287*, 15−27.
(14) Kobayashi, H.; Samukawa, K.; Nakayama, M.; Mandai, T.; Honma, I. Promoting Reversible Cathode Reactions in Magnesium Rechargeable Batteries Using Metastable Cubic $MgMn_2O_4$ Spinel Nanoparticles. *ACS Appl. Nano Mater.* **2021**, *4*, 8328−8333.
(15) Nakayama, M.; Kaneko, M.; Wakihara, M. First-Principles Study of Lithium Ion Migration in Lithium Transition Metal Oxides with Spinel Structure. *Phys. Chem. Chem. Phys.* **2012**, *14*, 13963−13970.
(16) Johnson, I. D.; Mistry, A. N.; Yin, L.; Murphy, M.; Wolfman, M.; Fister, T. T.; Lapidus, S. H.; Cabana, J.; Srinivasan, V.; Ingram, B. J. Unconventional Charge Transport in $MgCr_2O_4$ and Implications for Battery Intercalation Hosts. *J. Am. Chem. Soc.* **2022**, *144*, 14121−14131.
(17) Yin, J.; Brady, A. B.; Takeuchi, E. S.; Marschilok, A. C.; Takeuchi, K. J. Magnesium-Ion Battery-Relevant Electrochemistry of $MgMn_2O_4$: Crystallite Size Effects and the Notable Role of Electrolyte Water Content. *Chem. Commun.* **2017**, *53*, 3665−3668.
(18) Sone, K.; Hayashi, Y.; Mandai, T.; Yagi, S.; Oaki, Y.; Imai, H. Effective 3D Open-Channel Nanostructures of a $MgMn_2O_4$ Positive Electrode for Rechargeable Mg Batteries Operated at Room Temperature. *J. Mater. Chem. A* **2021**, *9*, 6851−6860.
(19) Kobayashi, H.; Yamaguchi, K.; Honma, I. Rapid Room-Temperature Synthesis of Ultrasmall Cubic Mg−Mn Spinel Cathode Materials for Rechargeable Mg-Ion Batteries. *RSC Adv.* **2019**, *9*, 36434−36439.
(20) Malik, R.; Zhou, F.; Ceder, G. Kinetics of Non-Equilibrium Lithium Incorporation in $LiFePO_4$. *Nat. Mater.* **2011**, *10*, 587−590.
(21) Kang, B.; Ceder, G. Battery Materials for Ultrafast Charging and Discharging. *Nature* **2009**, *458*, 190−193.
(22) Bayliss, R. D.; Key, B.; Sai Gautam, G.; Canepa, P.; Kwon, B. J.; Lapidus, S. H.; Dogan, F.; Adil, A. A.; Lipton, A. S.; Baker, P. J.; Ceder, G.; Vaughey, J. T.; Cabana, J. Probing Mg Migration in Spinel Oxides. *Chem. Mater.* **2020**, *32*, 663−670.
(23) Liu, M.; Rong, Z.; Malik, R.; Canepa, P.; Jain, A.; Ceder, G.; Persson, K. A. Spinel Compounds as Multivalent Battery Cathodes: A Systematic Evaluation Based on ab initio Calculations. *Energy Env. Sci.* **2015**, *8*, 964−974.
(24) Rong, Z.; Malik, R.; Canepa, P.; Sai Gautam, G.; Liu, M.; Jain, A.; Persson, K.; Ceder, G. Materials Design Rules for Multivalent Ion Mobility in Intercalation Structures. *Chem. Mater.* **2015**, *27*, 6016−6021.
(25) Kwon, B. J.; Yin, L.; Park, H.; Parajuli, P.; Kumar, K.; Kim, S.; Yang, M.; Murphy, M.; Zapol, P.; Liao, C.; Fister, T. T.; Klie, R. F.; Cabana, J.; Vaughey, J. T.; Lapidus, S. H.; Key, B. High Voltage Mg-Ion Battery Cathode via a Solid Solution Cr−Mn Spinel Oxide. *Chem. Mater.* **2020**, *32*, 6577−6587.
(26) Canepa, P.; Sai Gautam, G.; Hannah, D. C.; Malik, R.; Liu, M.; Gallagher, K. G.; Persson, K. A.; Ceder, G. Odyssey of Multivalent Cathode Materials: Open Questions and Future Challenges. *Chem. Rev.* **2017**, *117*, 4287−4341.
(27) Ichitsubo, T.; Okamoto, S.; Kawaguchi, T.; Kumagai, Y.; Oba, F.; Yagi, S.; Goto, N.; Doi, T.; Matsubara, E. Toward "rocking-chair type" Mg−Li dual-salt batteries. *J. Mater. Chem. A* **2015**, *3*, 10188−10194.
(28) Okubo, M.; Mizuno, Y.; Yamada, H.; Kim, J.; Hosono, E.; Zhou, H.; Kudo, T.; Honma, I. Fast Li-Ion Insertion into Nanosized $LiMn_2O_4$ without Domain Boundaries. *ACS Nano* **2010**, *4*, 741−752.
(29) Yokozaki, R.; Kobayashi, H.; Honma, I. Reductive Solvothermal Synthesis of $MgMn_2O_4$ Spinel Nanoparticles for Mg-Ion Battery Cathodes. *Ceram. Int.* **2021**, *47*, 10236−10241.
(30) Miyamoto, Y.; Kuroda, Y.; Uematsu, T.; Oshikawa, H.; Shibata, N.; Ikuhara, Y.; Suzuki, K.; Hibino, M.; Yamaguchi, K.; Mizuno, N. Rational Low-Temperature Synthesis of Ultrasmall Nanocrystalline Manganese Binary Oxide Catalysts under Controlled Metal Cation Hydration in Organic Media. *ChemNanoMat* **2016**, *2*, 297−306.
(31) Nakai, S.; Uematsu, T.; Ogasawara, Y.; Suzuki, K.; Yamaguchi, K.; Mizuno, N. Aerobic Oxygenation of Alkylarenes over Ultrafine Transition-Metal-Containing Manganese-Based Oxides. *ChemCatChem.* **2018**, *10*, 1096−1106.

https://doi.org/10.1021/acsnano.2c12392
ACS Nano 2023, 17, 3135−3142

(32) Fukasawa, T.; Ando, M.; Ohji, T.; Kanzaki, S. Synthesis of Porous Ceramics with Complex Pore Structure by Freeze-Dry Processing. *J. Am. Ceram. Soc.* **2001**, *84*, 230−232.
(33) Stunda-Zujeva, A.; Irbe, Z.; Berzina-Cimdina, L. Controlling the Morphology of Ceramic and Composite Powders Obtained via Spray Drying − A Review. *Ceram. Int.* **2017**, *43*, 11543−11551.
(34) Julien, C. M.; Massot, M. Lattice Vibrations of Materials for Lithium Rechargeable Batteries I. Lithium Manganese Oxide Spinel. *Mater. Sci. Eng., B* **2003**, *97*, 217−230.
(35) Malavasi, L.; Galinetto, P.; Mozzati, M. C.; Azzoni, C. B.; Flor, G. Raman Spectroscopy of AMn_2O_4 (A = Mn, Mg and Zn) Spinels. *Phys. Chem. Chem. Phys.* **2002**, *4*, 3876−3880.
(36) Iimura, R.; Kobayashi, H.; Honma, I. Suppressing Electrolyte Decomposition at Cathode/Electrolyte Interface by Mg-Fe Binary Oxide Coating towards Room-Temperature Magnesium Rechargeable Battery Operation. *Electrochemistry* **2022**, *90*, 067002.
(37) Yagi, S.; Ichikawa, Y.; Yamada, I.; Doi, T.; Ichitsubo, T.; Matsubara, E. Synthesis of Binary Magnesium−Transition Metal Oxides via Inverse Coprecipitation. *Jpn. J. Appl. Phys.* **2013**, *52*, 025501.
(38) van de Walle, A.; Asta, M.; Ceder, G. The Alloy Theoretic Automated Toolkit: A User Guide. *Calphad* **2002**, *26*, 539−553.
(39) Aydinol, M. K.; Kohan, A. F.; Ceder, G.; Cho, K.; Joannopoulos, J. Ab initio Study of Lithium Intercalation in Metal Oxides and Metal Dichalcogenides. *Phys. Rev. B* **1997**, *56*, 1354−1365.
(40) Blöchl, P. E. Projector Augmented-Wave Method. *Phys. Rev. B* **1994**, *50*, 17953−17979.
(41) Perdew, J. P.; Burke, K.; Ernzerhof, M. Generalized Gradient Approximation Made Simple. *Phys. Rev. Lett.* **1996**, *77*, 3865−3868.
(42) Perdew, J. P.; Ruzsinszky, A.; Csonka, G. I.; Vydrov, O. A.; Scuseria, G. E.; Constantin, L. A.; Zhou, X.; Burke, K. Restoring the Density-Gradient Expansion for Exchange in Solids and Surfaces. *Phys. Rev. Lett.* **2008**, *100*, 136406.
(43) Kresse, G.; Furthmüller, J. Efficient Iterative Schemes for ab initio Total-Energy Calculations Using a Plane-Wave Basis Set. *Phys. Rev. B* **1996**, *54*, 11169−11186.
(44) Kresse, G.; Furthmüller, J. Efficiency of ab-initio Total Energy Calculations for Metals and Semiconductors Using a Plane-Wave Basis Set. *Comput. Mater. Sci.* **1996**, *6*, 15−50.
(45) Jain, A.; Hautier, G.; Ong, S. P.; Moore, C. J.; Fischer, C. C.; Persson, K. A.; Ceder, G. Formation Enthalpies by Mixing GGA and GGA + U Calculations. *Phys. Rev. B* **2011**, *84*, 045115.
(46) Morgan, D.; Van der Ven, A.; Ceder, G. Li Conductivity in Li_xMPO_4 (M = Mn, Fe, Co, Ni) Olivine Materials. *Electrochem. Solid-State Lett.* **2004**, *7*, A30.
(47) Miyamoto, Y.; Kuroda, Y.; Uematsu, T.; Oshikawa, H.; Shibata, N.; Ikuhara, Y.; Suzuki, K.; Hibino, M.; Yamaguchi, K.; Mizuno, N. Synthesis of Ultrasmall Li−Mn Spinel Oxides Exhibiting Unusual Ion Exchange, Electrochemical and Catalytic Properties. *Sci. Rep.* **2015**, *5*, 15011.
(48) Izumi, F.; Momma, K. Three-Dimensional Visualization in Powder Diffraction. *Solid State Phenom* **2007**, *130*, 15−20.
(49) Ravel, B.; Newville, M. ATHENA, ARTEMIS, HEPHAESTUS: Data Analysis for X-Ray Absorption Spectroscopy Using IFEFFIT. *J. Synchrotron Rad.* **2005**, *12*, 537−541.
(50) Mandai, T. Critical Issues of Fluorinated Alkoxyborate-Based Electrolytes in Magnesium Battery Applications. *ACS Appl. Mater. Interfaces* **2020**, *12*, 39135−39144.

https://doi.org/10.1021/acsnano.2c12392
ACS Nano 2023, 17, 3135−3142